



**AFRL-RX-WP-JA-2017-0214**

**CHARACTERIZATION OF THE MICROSTRUCTURE OF THE  
COMPOSITIONALLY COMPLEX ALLOY  $\text{Al}_1\text{MoNb}_1\text{Ta}_{0.5}\text{Ti}_1\text{Zr}_1$   
(POSTPRINT)**

**O.N. Senkov**

**AFRL/RX**

**J.K. Jensen, B.A. Welk, R.E.A. Williams, J.M. Sosa, D.E. Huber, G.B. Viswanathan, and  
H.L. Fraser**

**Ohio State University**

**29 September 2016  
Interim Report**

**Distribution Statement A.  
Approved for public release: distribution unlimited.**

**© 2016 ELSEVIER LTD**

**(STINFO COPY)**

**AIR FORCE RESEARCH LABORATORY  
MATERIALS AND MANUFACTURING DIRECTORATE  
WRIGHT-PATTERSON AIR FORCE BASE, OH 45433-7750  
AIR FORCE MATERIEL COMMAND  
UNITED STATES AIR FORCE**

REPORT DOCUMENTATION PAGE				Form Approved OMB No. 0704-0188	
<p>The public reporting burden for this collection of information is estimated to average 1 hour per response, including the time for reviewing instructions, searching existing data sources, gathering and maintaining the data needed, and completing and reviewing the collection of information. Send comments regarding this burden estimate or any other aspect of this collection of information, including suggestions for reducing this burden, to Department of Defense, Washington Headquarters Services, Directorate for Information Operations and Reports (0704-0188), 1215 Jefferson Davis Highway, Suite 1204, Arlington, VA 22202-4302. Respondents should be aware that notwithstanding any other provision of law, no person shall be subject to any penalty for failing to comply with a collection of information if it does not display a currently valid OMB control number. <b>PLEASE DO NOT RETURN YOUR FORM TO THE ABOVE ADDRESS.</b></p>					
1. REPORT DATE (DD-MM-YY) 29 September 2016		2. REPORT TYPE Interim		3. DATES COVERED (From - To) 19 March 2014 – 29 August 2016	
4. TITLE AND SUBTITLE CHARACTERIZATION OF THE MICROSTRUCTURE OF THE COMPOSITIONALLY COMPLEX ALLOY $Al_1MoNb_1Ta_{0.5}Ti_1Zr_1$ (POSTPRINT)				5a. CONTRACT NUMBER IN-HOUSE	
				5b. GRANT NUMBER	
				5c. PROGRAM ELEMENT NUMBER	
6. AUTHOR(S) 1) O.N. Senkov - AFRL/RX 2) J.K. Jensen, B.A. Welk, R.E.A. Williams, J.M. Sosa, D.E. Huber, G.B. Viswanathan, and H.L. Fraser - Ohio State University				5d. PROJECT NUMBER	
				5e. TASK NUMBER	
				5f. WORK UNIT NUMBER X0W6	
7. PERFORMING ORGANIZATION NAME(S) AND ADDRESS(ES) 1) AFRL/RX Wright Patterson AFB, OH 45433 2) Ohio State University 1305 Kinnear Rd Columbus, OH 43212				8. PERFORMING ORGANIZATION REPORT NUMBER	
9. SPONSORING/MONITORING AGENCY NAME(S) AND ADDRESS(ES) Air Force Research Laboratory Materials and Manufacturing Directorate Wright-Patterson Air Force Base, OH 45433-7750 Air Force Materiel Command United States Air Force				10. SPONSORING/MONITORING AGENCY ACRONYM(S) AFRL/RXCM	
				11. SPONSORING/MONITORING AGENCY REPORT NUMBER(S) AFRL-RX-WP-JA-2017-0214	
12. DISTRIBUTION/AVAILABILITY STATEMENT Distribution Statement A. Approved for public release: distribution unlimited.					
13. SUPPLEMENTARY NOTES PA Case Number: 88ABW-2016-4837; Clearance Date: 29 Sep 2016. This document contains color. Journal article published in Scripta Materialia. © 2016 Elsevier Ltd. The U.S. Government is joint author of the work and has the right to use, modify, reproduce, release, perform, display, or disclose the work. The final publication is available at <a href="http://dx.doi.org/10.1016/j.scriptamat.2016.04.017">http://dx.doi.org/10.1016/j.scriptamat.2016.04.017</a>					
14. ABSTRACT (Maximum 200 words) Electron microscopy, X-ray energy dispersive spectroscopy, and tomographic reconstructions were used to characterize a high entropy alloy predominantly composed of refractory elements. The intragranular microstructure was found to consist of a periodic two phase mixture, where a disordered bcc phase is aligned orthogonally in an ordered B2 phase. The phases were found to exhibit continuous lattice registry and an orientation relationship given by $\langle 100 \rangle_{bcc} // \langle 100 \rangle_{B2}$ , $\{001\}_{bcc} // \{001\}_{B2}$ . X-ray energy dispersive spectroscopy was used to determine the compositions of the phases, and spectral images were used in the tomographic reconstruction of the alloy to reveal the morphology and the elemental partitioning between phases.					
15. SUBJECT TERMS High entropy alloys; High resolution electron microscopy; Electron tomography; Phase transformations; Ordered compounds					
16. SECURITY CLASSIFICATION OF:			17. LIMITATION OF ABSTRACT: SAR	18. NUMBER OF PAGES 6	19a. NAME OF RESPONSIBLE PERSON (Monitor) Bill Song 19b. TELEPHONE NUMBER (Include Area Code) (937) 255-1351
a. REPORT Unclassified	b. ABSTRACT Unclassified	c. THIS PAGE Unclassified			



## Regular Article

# Characterization of the microstructure of the compositionally complex alloy $\text{Al}_1\text{Mo}_{0.5}\text{Nb}_1\text{Ta}_{0.5}\text{Ti}_1\text{Zr}_1$



J.K. Jensen<sup>a</sup>, B.A. Welk<sup>a</sup>, R.E.A. Williams<sup>b</sup>, J.M. Sosa<sup>a</sup>, D.E. Huber<sup>a,b</sup>, O.N. Senkov<sup>c</sup>, G.B. Viswanathan<sup>a</sup>, H.L. Fraser<sup>a,\*</sup>

<sup>a</sup> Center for the Accelerated Maturation of Materials, Department of Materials Science and Engineering, The Ohio State University, 1305 Kinnear Rd., Columbus, OH 43212, USA

<sup>b</sup> Center for Electron Microscopy and Analysis, Department of Materials Science and Engineering, The Ohio State University, 1305 Kinnear Rd., Columbus, OH 43212, USA

<sup>c</sup> Air Force Research Laboratory, Materials and Manufacturing Directorate, Wright-Patterson AFB, OH 45433, USA

## ARTICLE INFO

## Article history:

Received 10 March 2016

Received in revised form 13 April 2016

Accepted 13 April 2016

Available online 1 May 2016

## Keywords:

High entropy alloys

High resolution electron microscopy

Electron tomography

Phase transformations

Ordered compounds

## ABSTRACT

Electron microscopy, X-ray energy dispersive spectroscopy, and tomographic reconstructions were used to characterize a high entropy alloy predominantly composed of refractory elements. The intragranular microstructure was found to consist of a periodic two phase mixture, where a disordered *bcc* phase is aligned orthogonally in an ordered B2 phase. The phases were found to exhibit continuous lattice registry and an orientation relationship given by  $\langle 100 \rangle_{\text{bcc}} // \langle 100 \rangle_{\text{B2}}$ ,  $\{001\}_{\text{bcc}} // \{001\}_{\text{B2}}$ . X-ray energy dispersive spectroscopy was used to determine the compositions of the phases, and spectral images were used in the tomographic reconstruction of the alloy to reveal the morphology and the elemental partitioning between phases.

© 2016 Elsevier Ltd. All rights reserved.

In the recent past, multi-principal component or high entropy alloys (HEAs) have garnered significant interest in the field of materials science due to their potentially attractive balance of properties including high compressive strength and corrosion resistance [1–3]. HEAs have been defined as alloy systems composed of five or more principal elements in more or less equiatomic concentrations [4]. The preferential formation of solid solution phases has been observed despite the compositional complexity and was initially attributed to the high configurational entropy of mixing of the constituent elements in the alloy [4]. Other factors including enthalpy of mixing and constituent element atomic size difference, however, influence the stability of solid solutions and many HEA systems have been reported to contain ordered intermetallic phases and complex nanoscale microstructures consistent with phase separation and/or spinodal decomposition [1,5,6]. Because of the uncertainty in the role of entropy on the stability of these alloys, they are referred to here as compositionally complex alloys (CCA).

The development of a novel class of CCAs using predominately refractory elements has been recently explored for potential use in high temperature aerospace structural components [7–9]. One such alloy,  $\text{Al}_1\text{Mo}_{0.5}\text{Nb}_1\text{Ta}_{0.5}\text{Ti}_1\text{Zr}_1$  (composition in molar ratio), was reported as having high strength at elevated temperature ( $\sigma_{0.2} = 1600$  MPa at  $T = 800$  °C,  $\sigma_{0.2} = 745$  MPa at  $T = 1000$  °C) and a relatively low density

superior to commercially available Ni-base superalloys [8]. Characterization of the alloy was limited to X-ray diffraction (XRD) and scanning electron microscopy (SEM). The alloy was reported to contain two *bcc* phases with similar lattice parameters in a nanoscale interpenetrating microstructure that was difficult to resolve using only SEM micrographs. Since the morphology of these phases and the interconnected nature of the microstructural features are expected to play a substantial role in the deformation behavior and mechanical properties of the alloy,  $\text{Al}_1\text{Mo}_{0.5}\text{Nb}_1\text{Ta}_{0.5}\text{Ti}_1\text{Zr}_1$  has been characterized in more detail using transmission electron microscopy and tomographic reconstructions using X-ray energy dispersive spectroscopy (XEDS).

The samples of  $\text{Al}_1\text{Mo}_{0.5}\text{Nb}_1\text{Ta}_{0.5}\text{Ti}_1\text{Zr}_1$  used in this study were prepared by vacuum arc melting high purity metals (99.9–99.99%) in an inert argon atmosphere. Details of the alloy preparation are described elsewhere [10]. Following solidification and hot isostatic pressing, the sample was heat-treated at a temperature of 1400 °C for 24 h followed by furnace cooling at a rate of 10 °C/min to room temperature in flowing argon. The microstructure of the heat-treated sample was characterized using backscattered electron (BSE) imaging in an FEI Sirion scanning electron microscope (SEM). Electron backscatter diffraction (EBSD) was performed on CCA samples using an FEI XL-30 FEG SEM equipped with an EDAX Hikari high-speed EBSD camera. SEM and EBSD image processing and analysis was performed using the Materials Image Processing and Automated Reconstruction (MIPAR) software package [11]. TEM lamellae samples were prepared at site specific locations from the surface of the bulk sample, from  $\langle 001 \rangle$  oriented grains,

\* Corresponding author at: CAMM, The Ohio State University, 1305 Kinnear Rd., Suite 100, Columbus, OH 43212-1177, USA.

E-mail address: [fraser.3@osu.edu](mailto:fraser.3@osu.edu) (H.L. Fraser).

using an FEI Helios NanoLab 600 Dual-Beam focused ion beam (DB-FIB) instrument. The FIB lift-out and thinning procedures are described elsewhere [12].

The thinned FIB lamellae were characterized using conventional bright-field (BF) and dark-field (DF) TEM imaging in an FEI/Phillips CM200. Scanning transmission electron microscopy (STEM) high-angle annular dark-field (HAADF) micrographs were taken with an FEI Probe-Corrected Titan 80-300 STEM operating at 300 kV and a camera length of 115 mm. The convergence semiangle of the electron beam was 11.4 mrad and the inner and outer collection angles of the HAADF detector were 34.8 and 230.0 mrad, respectively. XEDS spectra were collected using an FEI Image-Corrected Titan 60-300 STEM equipped with a Super-X™ XEDS detector system. The TEM was operating with an accelerating voltage of 300 kV and an electron beam convergence semiangle of 25 mrad. Cliff-Lorimer quantification and analysis of Super-X™ XEDS data was performed using standardless native k-factors in the Bruker Esprit software.

The low magnification, BSE micrograph in Fig. 1(a) captures at least two distinct phases, one consisting of equiaxed grains, and the other phase, exhibiting dark contrast, present at some of the grain boundaries of the  $\text{Al}_1\text{Mo}_{0.5}\text{Nb}_1\text{Ta}_{0.5}\text{Ti}_1\text{Zr}_1$  sample. EBSD inverse pole figure (IPF) maps overlaid with image quality (IQ) micrographs, shown in Fig. 1(b), show that the equiaxed grains have a *bcc* crystal structure. The identity of the fairly coarse precipitation along the grain boundaries has not yet been confirmed. Low angle subgrain boundaries with misorientation angles of  $<1.5^\circ$  are present inside many grains (Fig. 1(a) and (b)). A BSE micrograph (Fig. 1(c)) recorded at higher magnification reveals fine precipitation of two phases in the equiaxed grains. These precipitates form a basket weave nanoscale structure inside the grains and become coarser at subgrain boundaries. The intragranular microstructure is identified by TEM to consist of a refined distribution of two interpenetrating phases, which appear to have a lamellar morphology (Fig. 1(d)).

Previously, the microstructure was characterized as consisting of two interpenetrating *bcc* phases [8]. As can be seen in Fig. 1(d), the selected area diffraction pattern (SADP) exhibits intensity maxima that appear to be superlattice reflections. Indeed, the DF-TEM micrograph of the refined, interpenetrating microstructure shown in the figure was recorded using the reflection circled in the diffraction pattern (inset), with the electron beam being nearly parallel to a  $\langle 001 \rangle$  zone axis. As can be seen, the microstructure appears to consist of a refined distribution of one phase, exhibiting dark contrast and consisting of cuboidal and stacked platelet precipitates  $\sim 40$  nm in edge length, aligned along  $\langle 100 \rangle$  directions, within a lighter contrast phase. Since the image is formed with an intensity maximum consistent with a superlattice reflection, it appears that the lighter phase is ordered. Given the locations of the superlattice reflections in this and other zone axes SADPs (not shown here), it is reasonable to conclude tentatively that the phase has the B2 crystal structure. In the SADP (Fig. 1(d)), the fundamental intensity maxima from both phases are coincident, and hence, within the error of measurement using SADPs, it appears that both phases have lattice parameters of  $\approx 0.329$  nm, indicating a reasonable degree of coherency between the two phases.

Fig. 2 (a and b) shows STEM-HAADF micrographs acquired with the electron beam parallel to the  $[001]$  zone axis of the *bcc*/B2 phases. The microstructure consists of two phases: one a cuboidal and plate-like precipitate phase, exhibiting grey contrast, aligned orthogonally in a phase which exhibits darker contrast. In STEM-HAADF imaging conditions, contrast arises from the collection of incoherently scattered high-angle electrons and, therefore, from variations in local atomic number between phases [13]. It follows that the grey phase has a higher average atomic number than the darker phase, as is confirmed by compositional analyses below. Fig. 2(b) shows a higher magnification STEM-HAADF image resolving atomic columns, in which the modulation of intensity from the corner site to the body centered site in the darker phase (i.e., the ordered phase) can be seen clearly. This is indicative of a

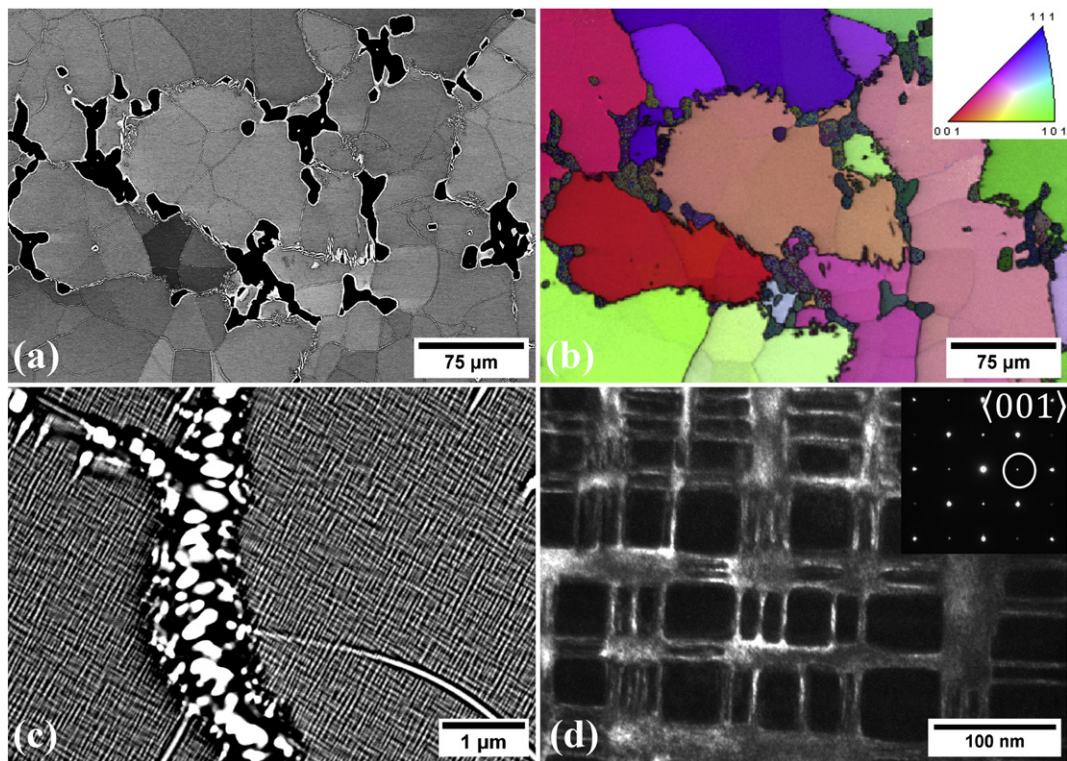
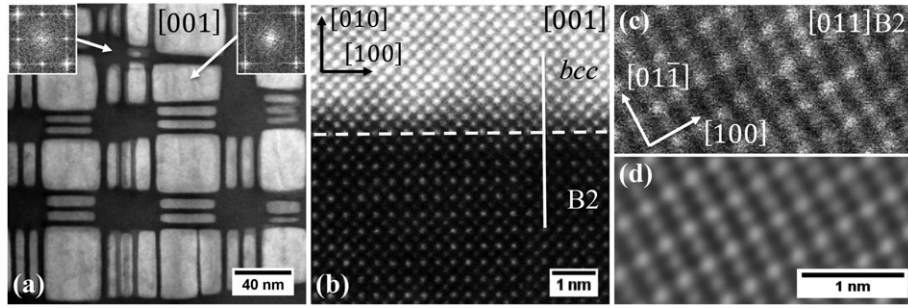


Fig. 1. (a) SEM BSE micrograph of the microstructure of  $\text{Al}_1\text{Mo}_{0.5}\text{Nb}_1\text{Ta}_{0.5}\text{Ti}_1\text{Zr}_1$  showing coarse grains, with intragranular features and dark intermetallic phases at the grain boundaries; (b) EBSD inverse pole figures with overlaid image quality map identifying the intragranular features as low angle subgrain boundaries; (c) SEM BSE micrograph showing intragranular microstructure near a low angle subgrain boundary; (d) TEM darkfield micrograph formed using the intensity maxima circled in the selected area diffraction pattern (inset).





**Fig. 2.** (a and b) STEM-HAADF micrographs acquired parallel to the [001] zone axis of the *bcc*/B2 phases with FFTs corresponding to the phases identified by the arrows. Unfiltered (c) and FFT-filtered (d) STEM-HAADF micrographs resolving atomic columns parallel to the [011] zone axis of the B2 phase.

difference in sublattice composition between the two atomic positions. The respective fast Fourier transform (FFT) of the darker phase (inserted in Fig. 2(a)) also shows spatial frequencies corresponding to ordering, further suggesting that the dark phase has the ordered B2 structure. The lighter cuboidal phase, delineated from the B2 phase by the horizontal dashed line, shows no apparent change in intensity between the corner and body centered sites. The respective FFT, inserted in the figure, is consistent with the phase being a *bcc* solid solution. The orientation relationship (OR) between the two phases is  $\langle 100 \rangle_{bcc} // \langle 100 \rangle_{B2}$ ,  $\{001\}_{bcc} // \{001\}_{B2}$ , and there is continuous lattice registry between the two phases highlighted by the superimposed white vertical line shown in Fig. 2(b).

From the image in Fig. 2(b), it appears that the interface between the two phases is fairly coherent. Interestingly, the XRD study described in [8] suggested that there were two *bcc* phases with slightly different lattice parameters. Although it has been shown in the present study that one of the phases is ordered, it is important to comment on the

difference in lattice parameter measurements realized in bulk samples (XRD) vs. thin samples (STEM-HAADF). It is well known that relaxations in very thin foils can occur because of the proximity of the foil surfaces, and so it is possible that in the extremely thin sample (from which the image in Fig. 2(b) was recorded) such relaxations may have occurred, giving a more optimistic impression of the degree of coherency between the two phases than may actually exist in the bulk.

It has been stated above that the present results are consistent with the darker phase being ordered with the B2 crystal structure. In a recent study by Lu et al. [14] on an Alnico alloy, two ordered phases, B2 and L2<sub>1</sub>, were identified. These two ordered structures differ in the number of their sublattices, B2 having two whereas L2<sub>1</sub> has three. STEM-HAADF imaging with the beam parallel to a  $\langle 110 \rangle$  zone axis permits all three sublattices to be distinguished, and STEM-HAADF images recorded in this orientation are shown in Fig. 2(c), the image formed using the raw data, and in Fig. 2(d), showing the image optimized using an FFT-filter. The adjacent atomic columns exhibit a bi-modal modulation in

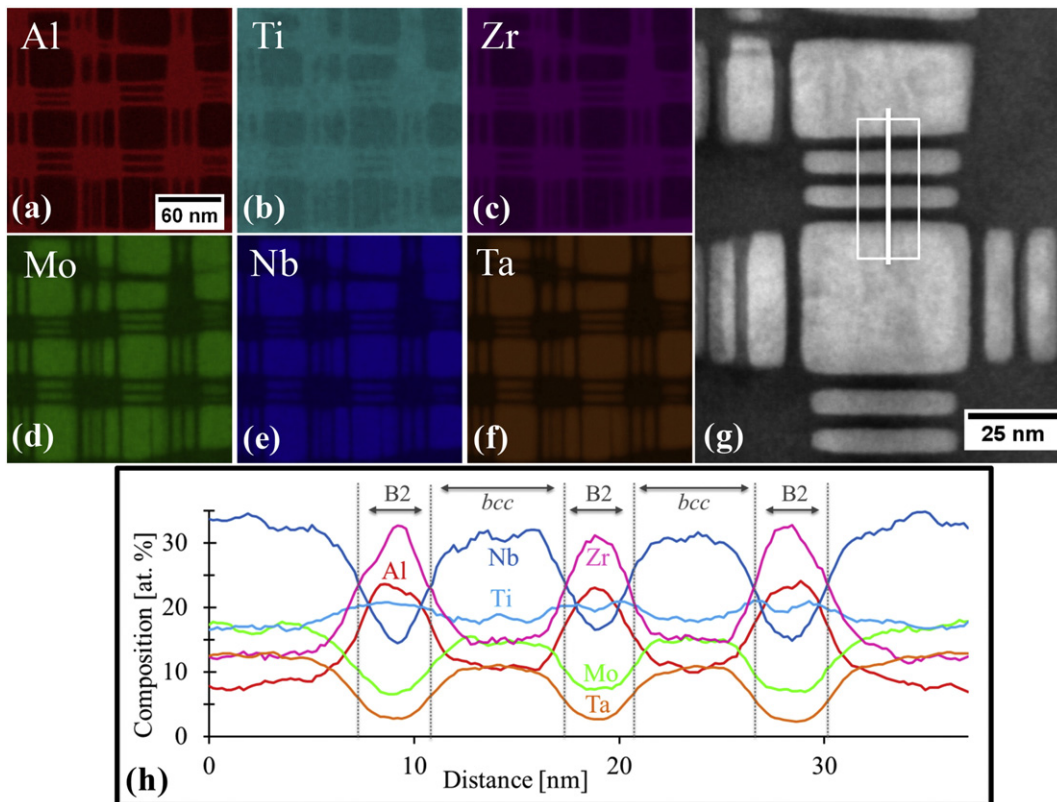


**Fig. 3.** (a–f) XEDS elemental maps of Al, Ti, Zr, Mo, Nb, and Ta, respectively, recorded in STEM using the Super-X™ detector. (g) A STEM-HAADF image with a white line identifying the location of the quantified XEDS line-scan shown in (h).

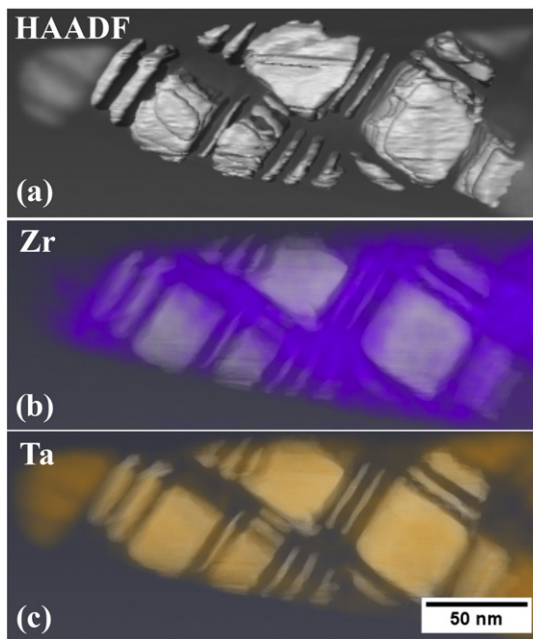


**Fig. 4.** (a) STEM-HAADF tomographic reconstruction of an  $\text{Al}_1\text{Mo}_{0.5}\text{Nb}_1\text{Ta}_{0.5}\text{Ti}_1\text{Zr}_1$  tapered needle with segmented cuboidal and platelet precipitates superimposed with (b and c) XEDS SI tomographic reconstructions of Zr and Ta elemental maps, respectively.

contrast, from which it is reasonable to conclude that there are only two sublattices. For these images to be consistent with the  $\text{L}_{21}$  structure, the average atomic numbers of the  $\text{B}_1$  and  $\text{B}_{11}$  sublattice would have to be essentially the same, and although this may be possible theoretically, in compositionally complex alloys, it seems rather unlikely. It is concluded here that both images are consistent with only two sublattices and the phase has the B2 structure.

As shown in Fig. 3 (a–f), a region of the ordered phase and disordered cuboidal phase microstructure was compositionally mapped in STEM using XEDS, as indicated in the figure. The elemental maps clearly show partitioning of Al, Zr, and Ti to the ordered phase and Ta, Mo, and Nb to the disordered *bcc* cuboidal and platelet precipitate phase. Fig. 3 (g) exhibits a STEM-HAADF image with a white line indicating from where the quantified elemental profiles (Fig. 3(h)) were recorded. The line profiles reveal a relatively sharp chemical interface between the two phases, when taking into account the fairly large convergence angle of the electron beam and other factors leading to beam spreading in the sample. Also, the profiles show similar compositions of the different morphologies of the disordered *bcc* phase. Quantification of the spectra was performed using the  $K_\alpha$  energies for Nb, Ti, Zr, and Al, the  $L_\alpha$  energy for Mo, and the  $M_\alpha$  energy for Ta to avoid overlapping peaks from known spurious X-ray sources, i.e. the Cu Omniprobe lift-out grid. Based on the quantification of the XEDS spectra, the composition of the ordered channel phase is approximately (in at.%)  $\text{Al}_{24}\text{Mo}_7\text{Nb}_{15}\text{Ta}_3\text{Ti}_{22}\text{Zr}_{29}$  and the disordered cuboidal phase is  $\text{Al}_8\text{Mo}_{18}\text{Nb}_{34}\text{Ta}_{13}\text{Ti}_{17}\text{Zr}_{10}$ . The average atomic number of the ordered and disordered phase is approximately 30 and 40, respectively, consistent with the contrast differences observed between the B2 phase and the disordered *bcc* solid solution phase in the STEM-HAADF images.

The morphology and distribution of the ordered and disordered phases of this CCA were deduced from 3D reconstructions of data obtained by electron tomography using a sample with a tapered needle geometry; both HAADF and XEDS signals were used to reconstruct the

object. In contrast to conventional FIB lamella geometry, the use of a tapered needle geometry in conjunction with a Fischione on-axis tomography holder allows for a full  $360^\circ$  of rotation without an increase in cross-sectional thickness of the sample or a risk of interference with the microscope pole piece. The tapered needle sample was prepared using a procedure described elsewhere [12]. The tomographic reconstructions using the STEM-HAADF and the Ta and Zr XEDS spectral images are shown in Fig. 4. The morphology of the disordered *bcc* phase, as shown in Fig. 4(a), is a mixture of stacked plate-like and cuboidal precipitates. It appears that the larger cuboidal precipitates are aligned such that each cube face is enclosed by a stack of two or three plate-like precipitates in a continuous channeled matrix of the ordered B2 phase. The reconstructions of the Zr and Ta XEDS maps, shown in Fig. 4(b) and (c) respectively, illustrate the partitioning of Zr to the ordered B2 phase and Ta to the disordered cuboidal and platelet precipitates. This 3D compositional variation was inherently difficult to observe through traditional 2D characterization, specifically the case of thin platelets in a stacked morphology where precipitate projection artifacts prevent accurate local 2D compositional measurements.

In summary, the microstructure had been previously mischaracterized as consisting of two *bcc* phases. Thus, it has been shown here that the microstructure consists of a disordered *bcc* phase and an ordered phase. Secondly, the ordered phase has the B2 structure rather than  $\text{L}_{21}$ . Thirdly, the two phases obey an OR given by  $\langle 100 \rangle_{\text{bcc}} // \langle 100 \rangle_{\text{B2}}, \{001\}_{\text{bcc}} // \{001\}_{\text{B2}}$ , and they are fairly coherent. This OR and the degree of coherency imply a microstructural formation mechanism involving phase separation. Fourthly, the compositions of the two phases have been determined and the chemical interface between the two phases is relatively sharp. Finally, the true morphology of the microstructures has been determined by electron tomography, and it has been shown that the microstructure may be described as a continuous channeled B2 phase with a discontinuous disordered *bcc* phase.

## Acknowledgements

The authors would like to acknowledge the financial support of the Dayton Area Graduate Studies Institute (DAGSI) program of the State of Ohio and the Air Force Research Laboratory, under program number RX0(1)-OSU-13-4. Work by ONS was supported through the Air Force on-site contract No. FA8650-15-D-5230 conducted by UES, Inc., Dayton, Ohio.

## References

- [1] Y. Zhang, Y.J. Zhou, J.P. Lin, G.L. Chen, P.K. Liaw, *Adv. Eng. Mater.* 10 (2008) 534–538.
- [2] C. Tong, M. Chen, S. Chen, J. Yeh, T. Shun, S. Lin, S. Chang, *Metall. Mater. Trans. A* 36 (2005) 1263–1271.
- [3] Y.J. Zhou, Y. Zhang, Y.L. Wang, G.L. Chen, *Appl. Phys. Lett.* 90 (2007).
- [4] J.-W. Yeh, S.-K. Chen, S.-J. Lin, J.-Y. Gan, T.-S. Chin, T.-T. Shun, C.-H. Tsau, S.-Y. Chang, *Adv. Eng. Mater.* 6 (2004) 299–303.
- [5] S. Singh, N. Wanderka, B.S. Murty, U. Glatzel, J. Banhart, *Acta Mater.* 59 (2011) 182–190.
- [6] B.A. Welk, R.E.A. Williams, G.B. Viswanathan, M.A. Gibson, P.A. Liaw, H.L. Fraser, *Ultramicroscopy* 134 (2013) 193–199.
- [7] O.N. Senkov, G.B. Wilks, D.B. Miracle, C.P. Chuang, P.K. Liaw, *Intermetallics* 18 (2010) 1758–1765.
- [8] O.N. Senkov, C. Woodward, D.B. Miracle, *JOM* 66 (2014) 2030–2042.
- [9] O.N. Senkov, S.V. Senkova, C. Woodward, D.B. Miracle, *Acta Mater.* 61 (2013) 1545–1557.
- [10] O.N. Senkov, S.V. Senkova, C. Woodward, *Acta Mater.* 68 (2014) 214–228.
- [11] J.M. Sosa, D.E. Huber, B. Welk, H.L. Fraser, *Integr. Mater. Manuf. Innov.* 3 (2014) 10.
- [12] J.M. Sosa, J.K. Jensen, D.E. Huber, G.B. Viswanathan, M.A. Gibson, H.L. Fraser, *Mater. Sci. Technol.* 31 (2015) 1250–1258.
- [13] S.J. Pennycook, *Ultramicroscopy* 30 (1989) 58–69.
- [14] P. Lu, L. Zhou, M.J. Kramer, D.J. Smith, *Sci. Rep.* 4 (2014) 3945.